Computational thermal-wave slice tomography with backpropagation and transmission reconstructions

Offer Padé[a] and Andreas Mandelis
Photothermal and Optoelectronic Diagnostics Laboratory, Department of Mechanical Engineering, University of Toronto, Toronto, Ontario M5S 1A4, Canada

(Received 25 February 1993; accepted for publication 7 September 1993)

Computational aspects of a new matrix equation-based thermal-wave subsurface diffraction tomographic method for object field reconstructions of transverse slices (planes) perpendicular to a material surface are presented. The method can be implemented on conventional workstations and mainframe computers. It uses the photothermally measured backpropagation (front detection) or transmission (back-surface detection) scanned thermal-wave field data in the solution of the Helmholtz thermal pseudowave equation, by solving the equivalent integral equation. The numerical computations of the inverse problem used in the slice image reconstruction were satisfactorily carried out via the Born approximation. Simulated thermal-wave tomographic data/case studies were used to evaluate the imaging characteristics of large-scale computational thermal-wave diffraction tomography as a quantitative measurement and nondestructive evaluation imaging discipline.

I. INTRODUCTION

Thermal-wave slice diffraction tomography (TSDT) was introduced as a photothermal imaging instrumentation technique[1–3] for the detection of subsurface defects in solid materials along cross-sectional planes perpendicular to the laser-beam scanned surface. The first TSDT instrument was based on contacting photopyroelectric tomographic detection[2,3] followed by ray-optic reconstruction of the cross-sectional thermal-wave image of the thermal diffusivity of the chosen slice.[2] The one-dimensional ray-optic based reconstruction technique was quite successful in illustrating the TSDT principle. However, using only ray-optic methods has many limitations, especially in highly dispersive wave fields, such as thermal waves. For this reason techniques familiar from x-ray cross-sectional tomography, such as the recovery of a 2D image from an oversampled 1D projection, cannot be applied to TSDT with satisfactory image contrast, spatial resolution, and low distortion.

Recently a full wave-field theoretical approach to TSDT was developed,[4] based on the spatial Laplace spectral decomposition of the thermal-wave object field. This approach is capable of deriving a Laplace slice theorem which links the transmission tomographic data in one dimension (the detector scan line) to the two-dimensional spatial Laplace transform of the cross-sectional slice image in the region between the photothermally excited material surface and the detector-scanned back surface. A problem with the computational implementation of the Laplace slice theorem is the fact that the thermal wave number is complex and at 45° to the real axis, which renders the Laplace transform inversion contours ill-defined in some circumstances. Therefore, the regular tomographic reconstructions of propagating wave fields[5] are not easily, if at all, applicable in practice to computational TSDT.

To circumvent the difficulty with ill-conditioned Laplace inversion contours, very recently we described a new rigorous matrix equation-based wave-field approach to the TSDT inversion problem.[6] Preliminary reconstructions of photopyroelectric thermal diffusivity tomograms showed that it is possible to obtain adequate reconstructions from a single column of thermal-wave data generated by a single laser position (sample front surface) and a scan of the localized detector (a metal pin capacitively coupled to the unelectroded pyroelectric element surface[7]) across a straight line on the back of the sample. In comparison, the matrix method yielded superior reconstructions to the ray-optic ones, obtained earlier[2,3] by the algebraic reconstruction technique (ART) used in x-ray tomography.[8] For the matrix method we used the Born approximation applied to the thermal-wave field propagation.[9] The method is further capable of solving the Helmholtz pseudowave equation[4] without recourse to Born's approximation, but with a higher degree of computer labor.

In this article we present a detailed comprehensive evaluation of computational slice diffraction tomography based on the matrix methodology of Ref. 6. The physical methodology is described and the computational technique allowing slice reconstruction and imaging is given for experimental situations involving both backpropagation as well as forward (transmission) thermal-wave data numerically manufactured from the solution to the direct problem (Helmholtz pseudowave equation[4]). A second generation instrument allowing experimental implementation sequentially of both backpropagation and transmission tomography by use of infrared radiometric scanning imaging is currently undergoing testing in our Laboratory and preliminary results will be reported in a near-future publication.

[a]On leave from Rafael, P.O. Box 2250, Haifa 31021, Israel.

II. MATHEMATICAL BACKGROUND

In the case of a harmonic photothermal excitation of a region of space, the temperature oscillation is found to obey the Helmholtz pseudowave equation[4,6,9]

$$[\nabla^2+\tilde{k}^2(r)]T(r)=0, \tag{1}$$

where

$$\tilde{k}(r)=(1-i)\left[\frac{\omega}{2\alpha(r)}\right]^{1/2}. \tag{2}$$

$\alpha(r)$ is the thermal diffusivity and ω is the angular frequency of the modulation of the laser-beam intensity. $\tilde{k}(r)$ is the complex thermal wave number. It was found that to be consistent with the experimental results, the thermal excitation should be described by the law $T(r,t)=T(r)e^{i\omega t}$. This sign selection of the exponent is important here, in contrast with conventional optical excitation, where the sign of the exponent is irrelevant due to the use of the second derivative with respect to time.

Upon defining[4]

$$F(r)\equiv\begin{cases}\tilde{k}_0^2[\nu^2(r)-1], & r\in R\\ 0, & r\notin R\end{cases} \tag{3}$$

the diffusion (Helmholtz pseudowave) equation takes the form[9]

$$(\nabla^2+\tilde{k}_0^2)T(r)=-F(r)T(r). \tag{4}$$

In Eq. (3) we defined R to be the object region and

$$\nu(r)=[\alpha_0/\alpha(r)]^{1/2} \tag{5}$$

with

$$\tilde{k}_0=(1-i)\left(\frac{\omega}{2\alpha_0}\right)^{1/2}\equiv k_0e^{-i\pi/4}. \tag{6}$$

α_0 is the diffusivity of the homogeneous (reference) region surrounding the object region R. The full solution of Eq. (4) satisfies in three dimensions[10,11]

$$T(r)=T_i(r)+\iiint_S G_0(r|\rho)F(\rho)T(\rho)d^3\rho + \iint_{\partial S}\left[G_0(r|\rho)\frac{\partial T}{\partial n_r}(\rho)-T(\rho)\frac{\partial G_0}{\partial n_r}\right]d\rho. \tag{7}$$

The integration is carried over the spatial region S which includes R, and its boundary ∂S. $\mathbf{n}_r$ is the normal unit vector to ∂S. In this work we assume that the region S is a cross-sectional slice in 2D space.[4] Moreover, we assume that S is a region of constant thickness, Fig. 1, and that the thermal excitation is on one side of the region ($y=0$), and the detection is either on the side of the thermal excitation (backscattering mode, $y=0$) or on the other side (transmission mode, $y=l=y_f$).

Furthermore we consider only the volume integral in Eq. (7). In earlier work[6] it was shown that neglecting the surface integral contribution to the transmitted photothermal signal is a good approximation in reconstructing the object field function of the cross-sectional area. However,

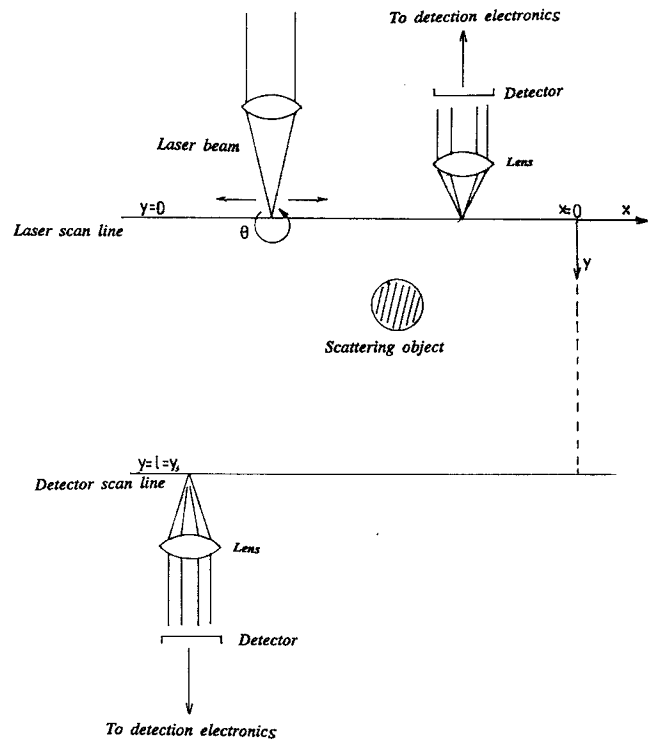

FIG. 1. Geometry for thermal-wave slice diffraction tomography amenable to backpropagation (BP) and transmission (T) detection. For each position of the laser-beam waist on the line $y=0$, the photothermal detector measures the thermal-wave field characteristics (amplitude and phase) along the back surface ($y=l$ line; transmission) or along the front surface in the vicinity of the laser beam spot ($y=0$ line; backpropagation). The region $0<y<y_f$ is the object region S.

this has not been proven rigorously and therefore the influence of the surface integral will be examined in more detail in an upcoming study. If the thermal-wave field $T(x,y=y_f)$ is measured (transmission mode), and if

$$T(r)=T_i(r)+T_s(r) \tag{8}$$

then using Eq. (7) we obtain along the object region of the 2D slice between $y=0$ and $y=y_f$, and between $x=x_i$, and $x=x_f$

$$T_s(x,y_f)=\int_{x_i}^{x_f}\int_0^{y_f} G_0[r(x,y_f)|\rho(\xi,\eta)] \times F[\rho(\xi,\eta)]T[\rho(\xi,\eta)]d\xi\, d\eta. \tag{9}$$

If the thermal-wave field $T(x,y=0)$ is measured (backpropagated mode), then

$$T_s(x,0)=\int_{x_i}^{x_f}\int_0^{y_f} G_0[r(x,0)|\rho(\xi,\eta)] \times F[\rho(\xi,\eta)]T[\rho(\xi,\eta)]d\xi\, d\eta. \tag{10}$$

Note that the surface integral contribution to the backscattered photothermal signal will also be neglected without proof. The adequacy of this approximation for the accuracy of reconstruction of the object field function will be examined via the various artificial situations to be described in what follows. Thus, it will be shown *a posteriori* that effective object field function reconstructions may be generated using only backscattered volume integral data in many situations corresponding to cases of practical interest and importance.

Although a rigorous justification of the omission of surface integrals in both backscattered and transmission modes still remains to be given, the physical plausibility of this approximation stems from the fact that the thermal-wave flux across the boundary, $\partial T/\partial n_r$ and $\partial G_0/\partial n_r$ in the integrand of Eq. (7), is essentially zero in the case where a solid sample is surrounded by air. Heat flux continuity across the solid/gas interface renders $\partial T/\partial n_r \propto k_g/k_s \simeq 10^{-3}$ for the great majority of solids. Here k_j is the thermal conductivity of medium (j).

In Eq. (10) G_0 is the two-dimensional thermal-wave Green's function for the region S, with the property[4,6]

$$G_0(r|\rho)=G_0(|r-\rho|) \tag{11}$$

provided that[10] the thermal-wave source point ρ and/or the observation point r are not infinitesimally close to the boundary ∂S which encloses the spatial region S.

In Ref. 6 we showed that Green's function for the two-dimensional thermal diffusion Helmholtz pseudowave Eq. (4) is

$$G_0(|r-\rho|)=\frac{i}{4}H_0^2(e^{i\pi/4}k_0|r-\rho|), \tag{12}$$

where H_0^2 is the Hankel function of the second kind of order zero.

III. THE COMPUTATIONAL METHOD FOR THE INVERSE PROBLEM

The conventional techniques used in electromagnetic or acoustic tomography for solving integral equations of the type of Eqs. (9) and (10) are by Fourier transform methods.[5] Usually one obtains the one-dimensional Fourier transform of T_s for every position of the exciting laser, and by using the Fourier slice theorem[5] it is possible to obtain a map of the inhomogeneity of the object. When thermal waves are involved, we deal with complex wave numbers, short paths of propagation of the waves leading to extreme near field approximations,[9,12] and the requirement for a generalized two-dimensional spatial Laplace transform inversion,[4] a nontrivial task. Furthermore, the fact that the movements of the laser and the detector apertures are limited to straight lines makes it necessary to utilize other methods for solving Eqs. (9) and (10). The ultrasonic experimental geometry in Ref. 13 is similar to the one described in Fig. 1. However, the method described in Ref. 13 uses only real values for $\tilde{k}_0$ in order to avoid inversion of Laplace transforms, a situation which is unavoidable with thermal waves. In this work we describe an efficient alternate computational technique for TSDT, based on matrix methods, rather than the well-known, but unwieldy in the thermal-wave case, Fourier transform methods.

The proposed technique is based on a special method of discretization of Eqs. (9) and (10). The sampled region ($y=y_f$ or $y=0$) is divided into n intervals, and the rectangular region

$$S=\{(x,y)\,|\,x_i\leqslant x\leqslant x_f;0\leqslant y\leqslant y_f\} \tag{13}$$

is divided into n^2 cells. Since Eqs. (9) and (10) are double integrals, the choice of n^2 points at the boundary is essential in order to obtain a square matrix.

Now, for $1\leqslant j\leqslant n$, Eq. (9) assumes the following form:

$$T_s(j\Delta x,y_f)=\int_{x_i}^{x_f}\int_0^{y_f} G_0[r(j\Delta x,y_f)\,|\,\rho(\xi,\eta)] \times F[\rho(\xi,\eta)]T[\rho(\xi,\eta)]d\xi\, d\eta \tag{14}$$

and Eq. (10) can be written in a similar form.

To obtain a discretized form of Eq. (14) we order the grid points in S, $(k\Delta\xi,l\Delta\eta)$ in the following matrix order $m(k,l)$:[6]

$$\begin{pmatrix} 1 & 2 & 6 & 7 & 15 & 16 & \cdot \\ 3 & 5 & 8 & 14 & 17 & \cdot & \\ 4 & 9 & 13 & 18 & \cdot & & \\ 10 & 12 & 19 & \cdot & & & \\ 11 & 20 & \cdot & & & & \\ 21 & \cdot & & & & & \\ \cdot & & & & & & \end{pmatrix}. \tag{15}$$

We chose the scheme of the matrix order (15) as our method of counting the cells in the inner region because this method is independent of the number of cells, i.e., it can be used for any value of n and it is easy to program.

Discretizing Eq. (14) by the rectangular rule,[14] we obtain

$$T_s(k\Delta x,y_f)=\sum_{m=1}^{n^2} G_0(|r_k-\rho_m|)F(\rho_m)T(\rho_m), \tag{16}$$

where

$$\rho_m=\rho_{m(i,j)}=\langle(i\Delta\xi)^2,(j\Delta\eta)^2\rangle \tag{17}$$

and the right-hand side of Eq. (17) indicates the norm of a vector with grid components $i\Delta\zeta$ and $j\Delta n$ measured from the origin.

Formally the left-hand side of Eq. (14) is known from the photothermal tomographic measurement,[2] where the amplitude and phase of the scattered field are measured. We use the complex form of T_s: $T_s=|T_s|e^{iv}$. The thermal-wave Green's function is also a complex quantity for the present problem and is given by Eq. (12).[6] Therefore, the complex-valued linear system (16) can be solved for the matrix FT (the multiplicity), which is the object function F multiplied by the complex temperature T. In this work we retain only the real part of the complex solution. At this stage we have the value of FT in the entire region S, so now we can calculate the scattered field in the entire region S, by

TABLE I. Computational flowcart for the calculation of the object function $F(r)$. (Note: $y_f/0$ indicates forward transmitted/backpropagated thermal-wave detection, respectively.)

Known (input) fields	Equation #	Computed field
$T_s(k\Delta x, y_f/0)$ (expt) $G_0(\|r-\rho\|)$ (theor)	$\longrightarrow$ (16) $\longrightarrow$	$F(\rho)T(\rho)$
$[F(\rho)T(\rho)]$ (comp) $G_0(\|r-\rho\|)$ (theor)	$\longrightarrow$ (18) $\longrightarrow$	$T_s(k\Delta x, l\Delta y)$
$T_s(k\Delta x, l\Delta y)$ (comp) $T_i(r)$ (theor)	$\longrightarrow$ (8) $\longrightarrow$	$T(r)$
$T(r)$ (comp) $G_0(\|r-\rho\|)$ (theor) $T_s(k\Delta x, y_f/0)$ (expt)	$\longrightarrow$ (16) $\longrightarrow$	$F(\rho)$

$$T_s(k\Delta x, l\Delta y) = \sum_{i=1}^{n} \sum_{j=1}^{n} G_0(|r_{k,l} - \rho_{m(i,j)}|) \times F(\rho_{m(i,j)}) T(\rho_{m(i,j)}). \tag{18}$$

Carrying out the double sum (18) for $0 \leqslant k,l \leqslant n$ results in obtaining the scattered field T_s in the entire cross-sectional region. Experimentally, a tomographic measurement provides the amplitude and the phase data of the transmitted field T and using Eq. (8) we obtain the scattered field T_s. Therefore inserting the newly calculated thermal-wave field T_s into Eq. (8) enables us to solve Eq. (16), now for the object function F. The solution of the complex linear system (16) is a complex function whose real part is the required object function F and its imaginary part is theoretically 0. Numerically it is not exactly 0 and its magnitude may serve as a measure for successful reconstruction. The computational flowchart is shown in Table I. The use of an $n^2 \times n^2$ matrix requires considerable computer resources. However, in the current state of computer development it is not a severe restriction. For example, the solution of Eq. (8) for $n=25$, which means a system of 625 equations with 625 unknowns, takes about an hour on the Sun4 workstation and it would take (without vectorization) about 300 s on the Convex 110.

In the flowchart of Table I the theoretically obtained fields are the Green's function, Eq. (12), and the incident field $T_i(r)$. The solution of the homogeneous Helmholtz pseudowave equation

$$(\nabla^2 + \tilde{k}_0^2) T_i(r) = 0 \tag{19}$$

for a point source on the $y=0$ boundary of the experimental configuration of Fig. 1, and for the thermal-wave propagation similar to a spherical wave, has been shown[6] to be

$$T_i(r) = \frac{1}{\sqrt{r}} H_{1/2}^2(\tilde{k}_0 r), \tag{20}$$

where $H_{1/2}^2$ is the Hankel function of the second kind of order 1/2.[15] In this work we adopted the first Born approximation,[5] namely, in Eq. (14) we used $T_i(r)$ instead of $T(r)$. Therefore, although it is entirely possible to solve the inverse problem exactly by following the flowchart of Table I, we solved Eq. (14) directly for $F(\rho)$, in order to simplify the large-scale computation and save computer time. In what follows it will be seen that the Born approximation allows for good quality tomographic reconstructions in a number of cases of interest for subsurface slice nondestructive defect imaging in solid materials. The adequacy of the Born approximation in TSDT was shown earlier in Ref. 6 by the reconstruction quality of the thermal diffusivity cross-sectional images. Nevertheless, no rigorous proof of the sufficiency of this approximation in TSDT has been constructed. The use of the first Born approximation is widespread in the related field of ultrasonic diffraction tomography.[5] In object field reconstruction using that technique, Mueller *et al.*[16] investigated the fidelity of the Born and Rytov approximations as functions of the relative size between the ultrasonic wavelength λ and the radius of a circular inhomogeneity (defect). They found that the Born and Rytov approximations give identical results for an inhomogeneity with radius equal to λ, and that excellent reconstruction fidelity holds for inhomogeneities, the ultrasonic velocity variation of which is up to, and in excess of, 10% of the velocity in the uniform surrounding medium. The Born approximation, however, exhibited significant distortions on object field reconstruction for object radius equal to 3λ.[16] From the point of view of this relative size criterion, the application of the Born approximation to TSDT is also justified, as the sizes of the examined subsurface defects in this work ($\sim$1 mm radius holes) are well within the thermal wavelength ranges $\rho_t = 2\pi/|\tilde{k}_0| = 2\pi/k_0 = (2\pi\alpha_0/f)^{1/2}$ in the surrounding material (aluminum): typically in the 10–100 Hz modulation frequency f range and with $\alpha_0 = 0.82$ cm^2/s,[17] one obtains 0.23 cm$\leqslant \lambda_t \leqslant$0.72 cm.

On the other hand, the literature lacks a universal and/or rigorous criterion for the threshold of the Born approximation breakdown with increasing magnitude of the perturbation in the measurable parameter, which may be introduced by a scatterer (defect). The method usually adopted in ultrasonic diffraction tomography is the *ad hoc* assumption of either the Born or the Rytov approximation,[18,19] and the *a posteriori* verification of the validity by comparing the reconstructed field with the (often known) geometry of the scatterer. To a certain extent this is the philosophy adopted in the present work. A forthcoming comparison between our TSDT reconstructed images with the exact methodology, Table I, and with the Born approximation is expected to produce the desired criterion for the justification of the use of perturbative approximations in thermal-wave diffraction tomography.

Now, let **L** be the following complex matrix:

$$L_{km} = G_0(|r_k - \rho_m|), \tag{21}$$

where $m = m(i,j)$ according to the scheme (15).

When calculating the solution of Eq. (16) we usually use the trapezoidal rule for integration because it has higher numerical accuracy (order 2) than the rectangular rule.

As a result of this calculation we obtain a matrix **B** defined as

$$B_{km}=B_{km(i,j)}=\begin{cases} L_{km(i,j)}, & 1<i,j<n \\ \frac{1}{2}L_{km(i,j)}, & 1\leqslant i\leqslant n, \quad j=1 \vee j=n; \quad 1\leqslant k\leqslant n^2 \\ \frac{1}{2}L_{km(i,j)}, & 1\leqslant j\leqslant n, \quad i=1 \vee i=n. \end{cases} \tag{22}$$

In some cases we use Simpson's rule for integration.[14] This rule has numerical order of accuracy 4 and hence we need fewer computer resources when using it. However, then we must consider only odd values of n.[6]

Using Simpson's rule and some tedious algebraic manipulations, we obtain a matrix $\mathbf{D}$ as follows:

$$D_{km}=D_{km(i,j)}=\begin{cases} \frac{16}{9}L_{km(i,j)}, & i=2i_e, \quad j=2j_e, \quad 1\leqslant i_e,j_e\leqslant (n-1)/2 \\ \frac{4}{9}L_{km(i,j)}, & i=2i_0+1, \quad j=2j_0+1, \quad 1\leqslant i_0,j_0\leqslant (n-3)/2 \\ \frac{8}{9}L_{km(i,j)}, & i=2i_e, \quad j=2j_0+1, \quad 1\leqslant i_e\leqslant (n-1)/2, \quad 1\leqslant j_0\leqslant (n-3)/2 \\ \frac{4}{9}L_{km(i,j)}, & i=2i_0+1, \quad j=2j_e, \quad 1\leqslant j_0\leqslant (n-3)/2, \quad 1\leqslant j_e\leqslant (n-1)/2 \\ \frac{4}{9}L_{km(i,j)}, & i=2l, \quad 1\leqslant l\leqslant (n-1)/2, \quad j=1 \vee j=n \\ \frac{4}{9}L_{km(i,j)}, & j=2l, \quad 1\leqslant l\leqslant (n-1)/2, \quad i=1 \vee i=n \\ \frac{2}{9}L_{km(i,j)}, & i=2l+1, \quad 1\leqslant l\leqslant (n-3)/2, \quad j=1 \vee j=n \\ \frac{2}{9}L_{km(i,j)}, & j=2l+1, \quad 1\leqslant l\leqslant (n-3)/2, \quad i=1 \vee i=n. \end{cases} \tag{23}$$

We have the following $n^2\times n^2$ system of linear equations

$$\mathbf{Af}=\mathbf{t}, \tag{24}$$

where $\mathbf{A}$ is either $\mathbf{L}$, $\mathbf{B}$, or $\mathbf{D}$, $\mathbf{f}=FT$, and $\mathbf{t}=T_s$.

The main problem with this method, from the computational point of view, is that the matrix G_0T_i is in many cases almost singular. To overcome this problem we can use either the Tykhonov regularization method or we can solve the system using SVD (singular value decomposition).[20] In this work we use mainly the Tykhonov regularization,[21,22] which amounts to minimizing the functional

$$\Phi(z)=\|\mathbf{A}z-\mathbf{t}\|_2+\sigma\Omega(z), \tag{25}$$

where σ is the regularization parameter and $\Omega(z)$ is a positive convex functional.[22] For simplicity and ease of computation, we chose $\Omega(z)$ to be

$$\Omega(z)=\|z\|_2=\sqrt{\sum_{i=1}^{n}|z_i|^2}, \tag{26}$$

where $\|\cdot\|_2$ is the usual Euclidean norm.

Minimization of the functional $\Phi(z)$ is equivalent to minimization of

$$\Psi(z)=\sum_{i=1}^{n}\left(\sum_{j=1}^{n}a_{ij}z_j-t_i\right)\left(\sum_{j=1}^{n}\bar{a}_{ij}\bar{z}_j-\bar{t}_i\right)+\sigma\sum_{i=1}^{n}z_i\bar{z}_i, \tag{27}$$

where bars indicate complex conjugation.

Differentiating with respect to the components of z we find that the minimum is obtained as the solution of the linear system (starred quantities denote adjoint matrices)

$$(\sigma\mathbf{I}+\mathbf{A}^*\mathbf{A})\mathbf{z}=\mathbf{A}^*\mathbf{t}. \tag{28}$$

The fact that in Green's function, Eq. (12), we have a complex argument which has a small absolute value (because of small thermal-wave numbers) becomes the source of the ill posedness of the linear system. H_0^2 has an essential singularity at the origin causing uncontrolled behavior of the function.

The initial field T_i, which is the solution of

$$(\nabla^2+\tilde{k}_0^2)T(r)=0 \tag{29}$$

is given by Eq. (20).

To solve the system (28) we use the eispack library[23] to compute the eigenvalues and the eigenvectors of the matrix $\mathbf{M}=\sigma\mathbf{I}+\mathbf{A}^*\mathbf{A}$. Let $\mathbf{V}$ be the matrix whose columns are the eigenvectors of $\mathbf{M}$, and let $\mathbf{E}$ be the diagonal matrix of the corresponding eigenvalues. Then, $\mathbf{M}^{-1}=\mathbf{V}\mathbf{E}^{-1}\mathbf{V}^*$. The elements of $\mathbf{E}\geqslant\sigma$. Therefore, as long as σ is kept within the computer accuracy one obtains a good inversion. This puts some constraints on the possible values of σ. However, when $\sigma\approx 10^{-11}$ we obtain quite accurate inversions. The minimal values that we tried for the SVD method of solution were much larger, on the order of 10^{-6}.

IV. SIMULATED TOMOGRAPHIC INVERSIONS

We produced simulated results by using the integrals, Eqs. (9) and (10), where we substitute T_i for T according to the Born approximation. To study various aspects of our TSDT reconstructions we used a known object function, usually an ellipse

$$F(x,y)=\begin{cases} 4; & \dfrac{(x-x_c)^2}{a^2}+\dfrac{(y-y_c)^2}{b^2}\leqslant 1 \\ 0; & \text{otherwise.} \end{cases} \tag{30}$$

Here x_c and y_c are the foci of the ellipse and a,b are its axes. The ellipse represents a hole drilled in aluminum, the latter being a rectangular sample.

The value 4 was chosen because it is approximately the ratio of the thermal diffusivities of aluminum and air according to Eq. (3). T_i was calculated using Eq. (20). As a result we obtained the scattered field at both (upper and lower) edges of the rectangular sample field R. We used these values of the scattered field as input data for the reconstruction of F, the object function. In this work we refer to the surface where the laser was positioned as *the front surface*. The measurements taken on the front surface are referred to as the backpropagation thermal-wave signal. The measurements taken at the opposite side to the front surface are referred to as the transmitted thermal-wave signal. The depth of the hole location is measured from the front surface. In all the presented results we used a low density grid, usually 10×10, which means that the number of equations in our linear system Eq. (24) was 100. This number was chosen to minimize computer time and still obtain good reconstructions. The particular sets of object functions and their reconstructions chosen for presentation and discussion in this work address the following fundamental aspects of TSDT:

(i) Back-propagation (BP) and transmission (T) object function tomograms from a (thermally) thick sample with one ellipsoidal defect close to the front surface, or with one defect close to the back surface; Figs. 2–7.

(ii) BP and T object function tomograms from a (thermally) intermediate sample with one subsurface ellipsoidal defect; Figs. 8–10.

(iii) BP and T object function tomograms from a (thermally) thin sample with one ellipsoidal defect close to the back surface, or with one ellipsoidal defect close to the front surface; Figs. 11–16.

(iv) The effect of varying laser beam intensity modulation frequency (i.e., thermal wave number) on the quality of the reconstruction from a fixed thickness sample; Figs. 14–20.

(v) BP and T object function tomograms from a sample with two ellipsoidal defects close to each other and at the same depth, and comparison with tomograms from two other ellipsoidal defects farther away from each other at the same depth; Figs. 21–26.

(vi) Finally, BP and T object function tomograms from two elliptic defects in different depths and locations such that there is a partial overlap with respect to the line of sight between the thermal-wave source and several detector positions. In this configuration two sets of such defect pairs were examined: one close to the front surface, Figs. 27–29, and another one close to the back surface, Figs. 30–32.

In most figures we present both a three-dimensional relief of the reconstructed (or the input) object function field and a two-dimensional top-down view of the field (tomogram).

In Fig. 2 we present the simulated object function $F(x,y)$ in a thick (6.4 mm) cross-sectional strip, Fig. 1, of aluminum (flat region) with an ellipsoidal hole (air gap)

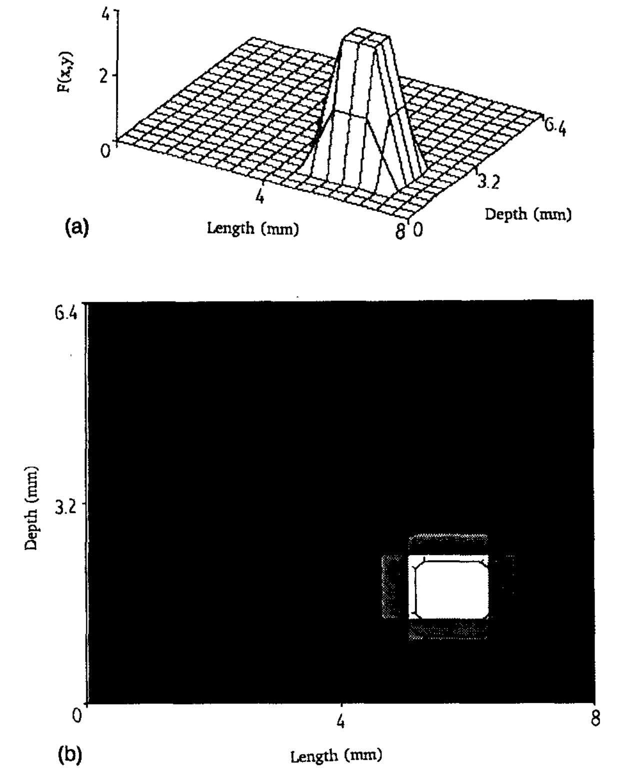

FIG. 2. (a) Three-dimensional relief of a simulated cross section of an aluminum strip of thickness 6.4 mm and width 8 mm, with an ellipsoidal hole centered at $(x_c,y_c)=(6\text{ mm}, 1.6\text{ mm})$; dimensions $(a,b)=(1\text{ mm}, 0.8\text{ mm})$. (b) Top-down view of the cross section, showing isometric contours.

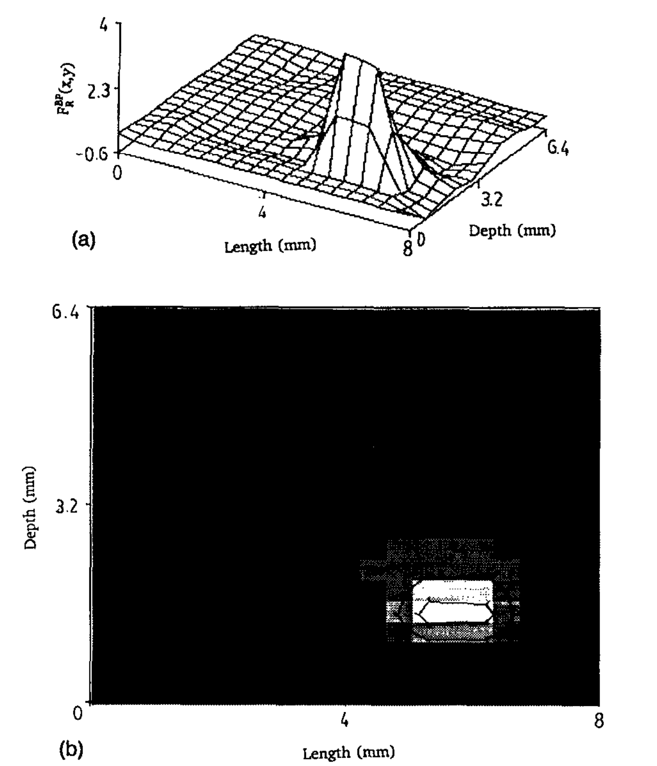

FIG. 3. (a) TSDT backpropagation reconstruction of the object function $F(x,y)$ of Fig. 2. Laser-beam position at $x_f=5$ mm (point source). Beam intensity modulation frequency: 30 Hz. Trapezoidal rule of integration using the Born approximation. (b) Top-down view showing isometric contours. Regularization parameter $\sigma=10^{-10}$.

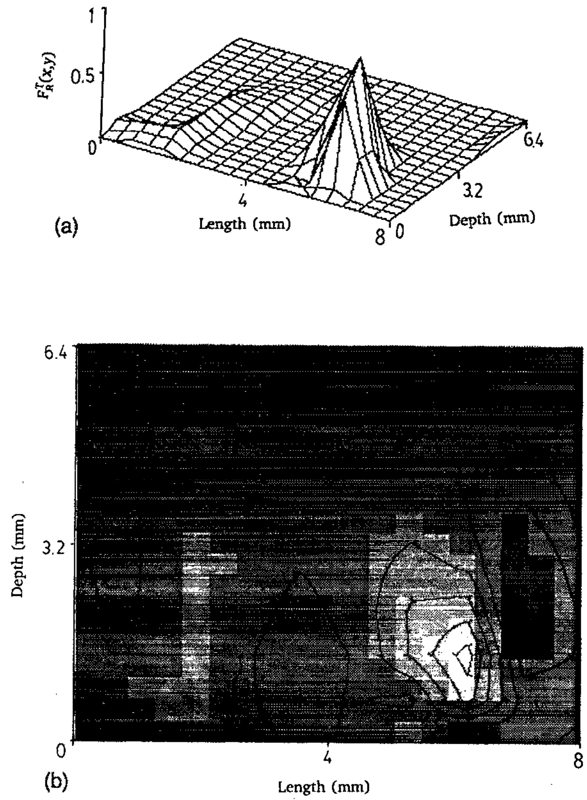

FIG. 4. (a) TSDT transmission reconstruction of the object function $F(x,y)$ of Fig. 2. Parameters similar to Fig. 3. (b) Top-down view showing isometric contours. Regularization parameter $\sigma = 10^{-6}$.

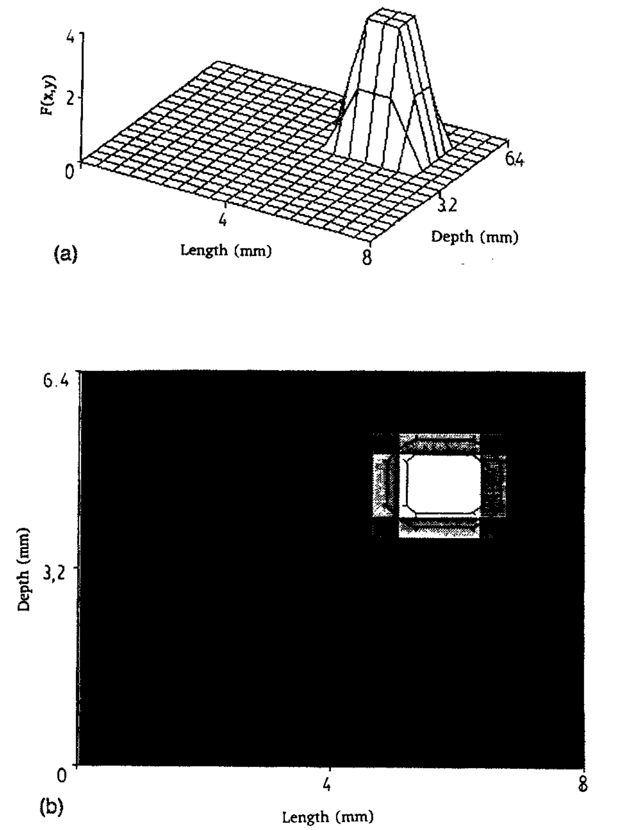

FIG. 5. (a) Three-dimensional relief of a simulated cross section of an aluminum strip of Fig. 3 with an ellipsoidal airgap hole centered at $(x_c, y_c) = (6\text{ mm}, 4.8\text{ mm})$; dimensions $(a,b) = (1\text{ mm}, 0.8\text{ mm})$. (b) Top-down view of the cross section, showing isometric contours.

close to the front surface. The defect region does not resemble an ellipse, but rather a pyramid due to the low grid resolution. This distortion is not inherent to our TSDT technique and can be readily rectified with finer grid resolution. The image contours in Fig. 2(b) and similar subsequent figures indicate isometric regions of the input object function, or of the reconstructed object function. Different grades of gray correspond to specific ranges of object function values, with brighter regions imaging higher values of the object function. Figure 3 shows the Born approximation based reconstruction, $F_R^{(BP)}(x,y)$, from the backscattered (BP) thermal-wave signal at 30 Hz. Although a single laser beam position was used, the reconstruction quality is very good when compared to Fig. 2 in both defect size, location, and magnitude (contrast). This is a remarkable improvement over the rather primitive, qualitative reconstructions of similar, near-front-surface hole defects we were able to perform previously[2] using the ray-optic algorithm ART.[8] The superior nature of the present wave-field approach is further strengthened upon noting that the data array required for a satisfactory Born reconstruction involves only *a single laser position*, $(1 \times m$ multiplexed data points) as opposed to a large number, k, of laser positions required by the ART algorithm $[(k \times m)$ multiplexed data points]. This feature reduces dramatically the total experimental scan time of TSDT. The same object function shown in Fig. 1 reconstructed from the transmitted (T) signal is shown in Fig. 4. Here, the quality of the tomogram is worse than under BP reconstruction, especially concerning the depth (y dimension) of the defect. This is mainly due to the thickness of the sample (6.4 mm), which, at $f = 30$ Hz, makes the sample thermally thick[24]

$$\sqrt{2}|\tilde{k}_0|^{-1} = 9.3 \times 10^{-2}\text{ cm} \ll l = 6.4 \times 10^{-1}\text{ cm}. \quad (31)$$

This condition implies a drastic decrease in the photothermal-wave disturbance magnitude due to the presence of the hole, especially since the defect lies near the laser-irradiated surface and far from the detector. For this reason the regularization parameter σ was 10^{-6} under T reconstruction, whereas we only needed $\sigma = 10^{-10}$ under BP reconstruction, Fig. 3. Large values of σ imply that the inverse problem is essentially ill conditioned, involving a substantial number of eigenvalues in the system (28), which are either zero or smaller than the computer's round-off error.

To study the effects of the depth position of a defect on the reconstruction, the ellipsoidal hole was subsequently located near the back surface of the 6.4 mm thick aluminum sample as shown in Fig. 5. Figures 6 and 7 are the reconstructions from the BP and T signals, respectively. It can be seen that the quality of these slice tomograms is seriously compromised as the result of the very deep location of the defect. The magnitude (contrast) is also degraded, while a number of artifacts appears in the near and extended neighborhood of the defect, especially in the BP case. It is important to note that, however degraded the

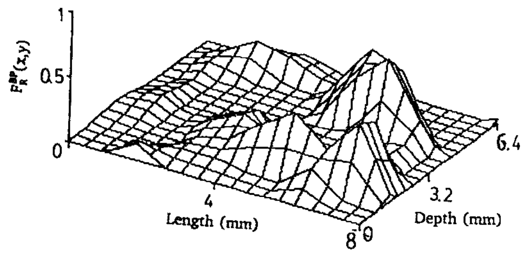

FIG. 6. TSDT backpropagation reconstruction of the object function $F(x,y)$ of Fig. 5. Laser-beam position at $x_f = 5$ mm (point source). Beam intensity modulation frequency: 30 Hz Trapezoidal rule of integration using the Born approximation. Regularization parameter $\sigma = 10^{-5}$.

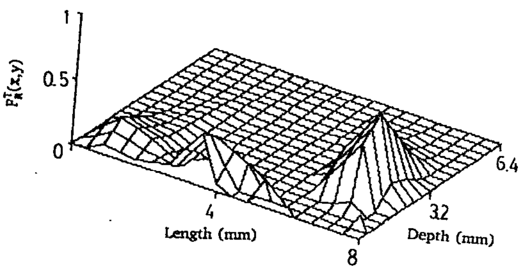

FIG. 7. TSDT transmission reconstruction of the object function $F(x,y)$ of Fig. 5. Parameters similar to Fig. 6. Regularization parameter $\sigma = 10^{-3}$, used for the best possible result.

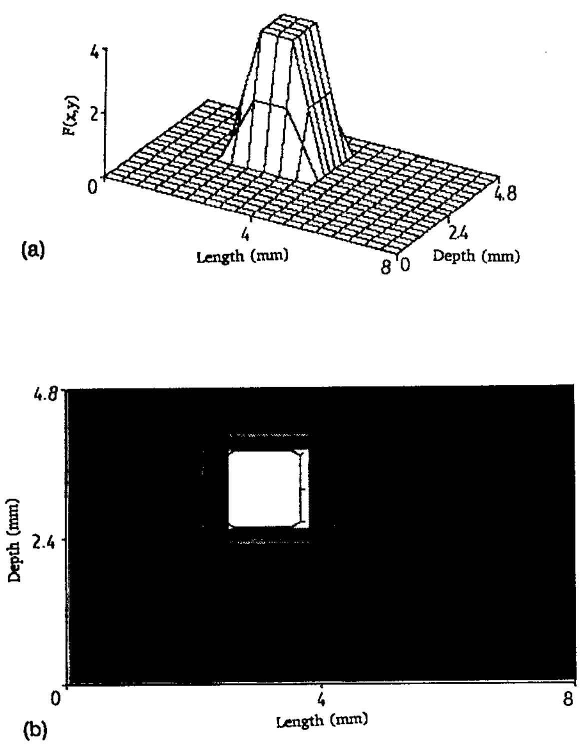

FIG. 8. (a) Three-dimensional relief of a simulated cross section of an aluminum strip of thickness 4.8 mm and width 8 mm, with an ellipsoidal airgap hole centered at $(x_c, y_c) = (3$ mm, 3.2 mm$)$; dimensions $(a,b) = (1$ mm, 0.8 mm$)$. (b) Top-down view of the cross section, showing isometric contours.

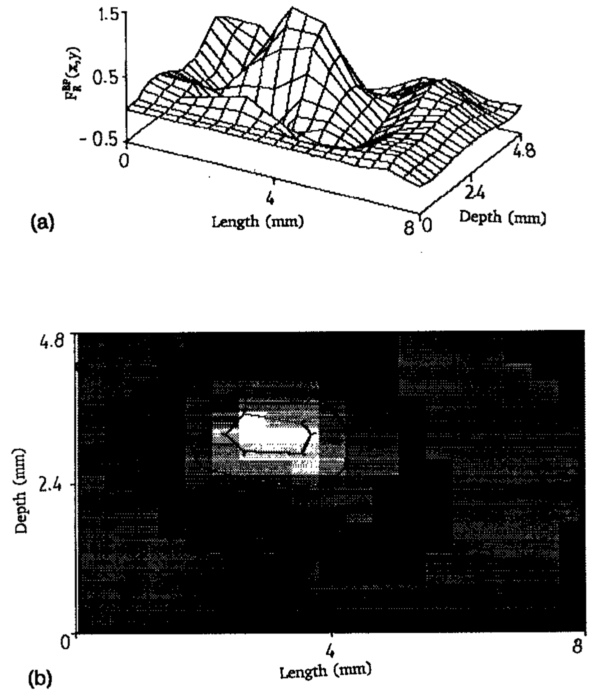

FIG. 9. TSDT backpropagation reconstruction of the object function $F(x,y)$ of Fig. 8. Laser-beam position at $x_f = 2$ mm (point source). Beam intensity modulation frequency: 30 Hz. Trapezoidal rule of integration using the Born approximation. (b) Top-down view showing isometric contours. Regularization parameter $\sigma = 10^{-9}$.

quality of the BP tomogram may be, the subsurface location of the airgap defect is reconstructed quite accurately. On the other hand, the T tomogram gives a reconstruction with the defect position shifted upwards and sideways. A comparison of tomogram reconstructions of shallow and deep defects in thick solids, Figs. 2–7, clearly shows that the BP mode is better than the T mode and produces high quality, high contrast tomograms of shallow defects. This mode also requires the lowest value of the regularization parameter σ.

An intermediate thickness sample ($l = 4.8$ mm) has also been considered in Figs. 8–10. The input cross-sectional object function which includes one ellipsoidal defect at intermediate depth is shown in Fig. 8. The BP reconstruction of Fig. 8, shown in Fig. 9, is of good quality and satisfactory contrast, despite the artifacts which appear in the background. A comparison between the input and reconstructed top-down views, Figs. 8(b) and 9(b),

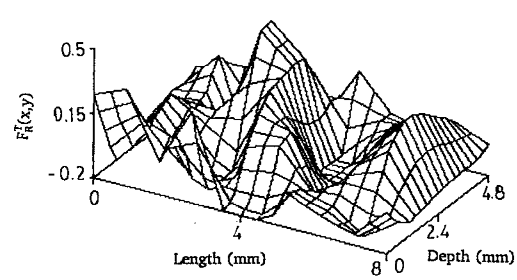

FIG. 10. TSDT transmission reconstruction of the object function $F(x,y)$ of Fig. 8. Parameters similar to Fig. 9. Regularization parameter $\sigma = 10^{-7}$.

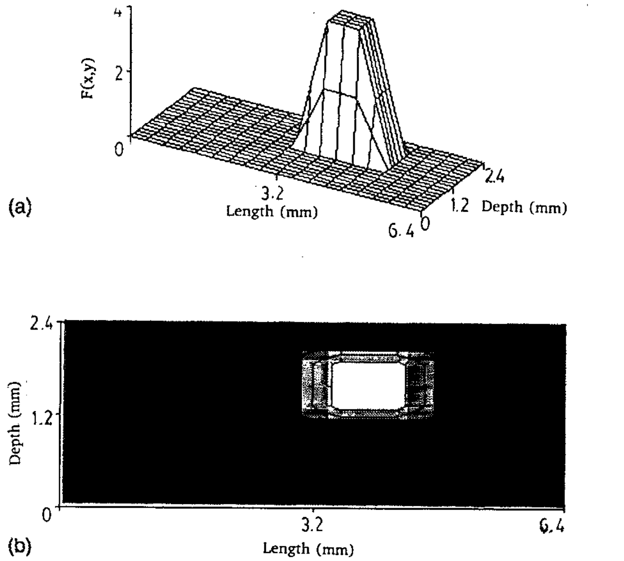

FIG. 11. (a) Three-dimensional relief of a simulated cross section of an aluminum strip of thickness 2.4 mm and width 6.4 mm, with an ellipsoidal airgap hole centered at $(x_c, y_c) = (4\ \text{mm}, 1.6\ \text{mm})$; dimensions $(a,b) = (0.8\ \text{mm}, 0.4\ \text{mm})$. (b) Top-down view of the cross section, showing isometric contours.

reveals the accurate reproduction of the hole location and boundaries. The good quality of the BP tomogram is further corroborated by the small σ value needed for reconstruction. The T reconstruction, Fig. 10, exhibits very high contrast of the defect, but is overall degraded, surrounded by several artifacts constituting noise. The fact that the sample thickness is less than that of Fig. 7 by 1.6 mm apparently makes an enormous difference in the ability of the T tomogram to reconstruct deep defects. The main reason for that is, of course, the existence of a high enough thermal-wave signal amplitude in the case illustrated by

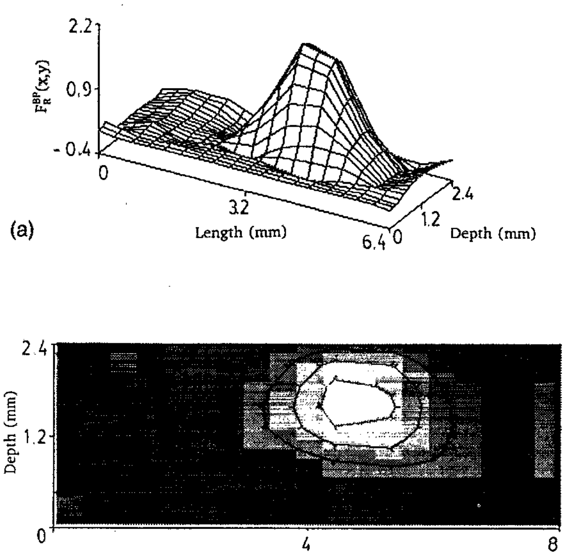

FIG. 12. (a) TSDT backpropagation reconstruction of the object function $F(x,y)$ of Fig. 11. Laser-beam position at $x_f = 3$ mm (point source). Beam intensity modulation frequency: 30 Hz. Trapezoidal rule of integration using the Born approximation. (b) Top-down view showing isometric contours. Regularization parameter $\sigma = 10^{-9}$.

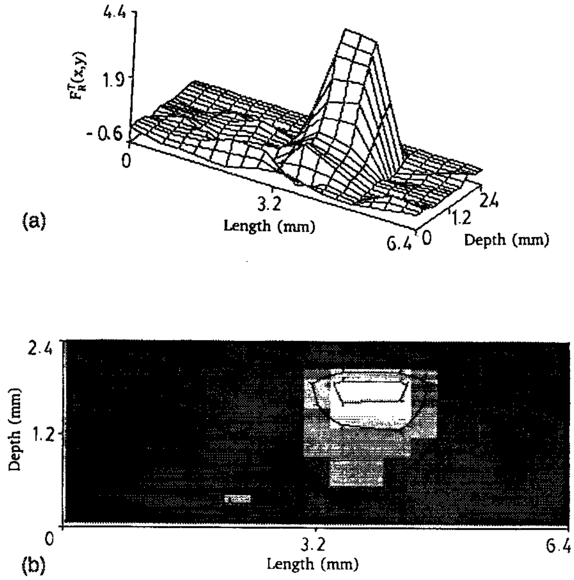

FIG. 13. (a) TSDT transmission reconstruction of the object function $F(x,y)$ of Fig. 11. Parameters similar to Fig. 12. (b) Top-down view showing isometric contours. Regularization parameter $\sigma = 0$.

Fig. 10 for our computational algorithm to discriminate signal elements successfully against the background, as was the case in Fig. 7.

Finally, we considered a narrow strip of aluminum of thickness $l = 2.4$ mm and located an ellipsoidal airgap defect close to the back surface, Figs. 11–13, and subsequently close to the front surface, Figs. 14–16. The object function of the strip with the deep defect is shown in Fig. 11. Figure 12 shows the BP tomogram exhibiting good contrast. It is interesting to note in Fig. 12(b) that the size of the reconstructed hole is bigger than its actual size, Fig. 11(b). This distortion (broadening) may be due to the omission of the surface integral term in Eq. (7), which

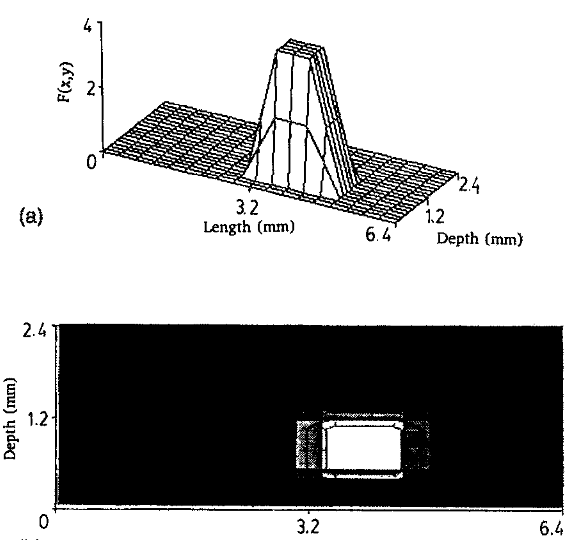

FIG. 14. (a) Three-dimensional relief of a simulated cross section of an aluminum strip of thickness 2.4 mm and width 6.4 mm, with an ellipsoidal airgap hole centered at $(x_c, y_c) = (4\ \text{mm}, 0.8\ \text{mm})$; dimensions $(a,b) = (0.8\ \text{mm}, 0.4\ \text{mm})$. (b) Top-down view of the cross section, showing isometric contours.

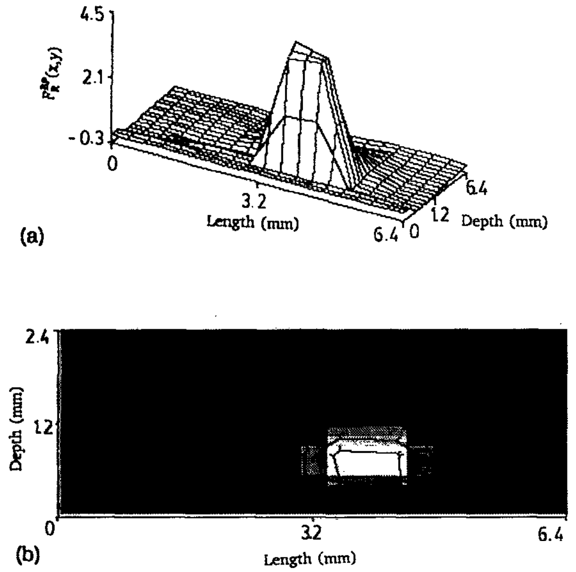

FIG. 15. (a) TSDT back-propagation reconstruction of the object function $F(x,y)$ of Fig. 14. Laser-beam position at $x_f=3$ mm (point source). Beam intensity modulation frequency: 30 Hz. Trapezoidal rule of integration using the Born approximation. (b) Top-down view showing isometric contours. Regularization parameter $\sigma=10^{-9}$.

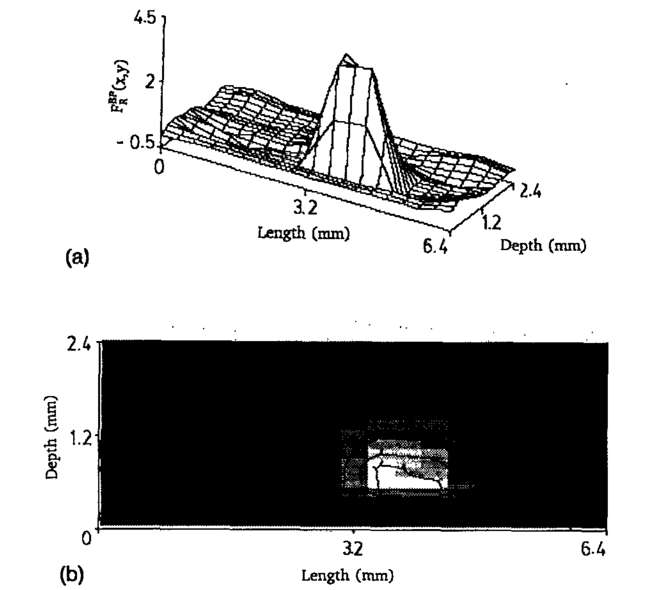

FIG. 17. Similar to Fig. 15 with beam intensity modulation frequency equal to 80 Hz. Regularization parameter $\sigma=10^{-9}$.

may have a nonvanishing contribution in thin strips, where thermal-wave reflections from the back surface after a single transit through l may have an effect on the value of the thermal-wave field in the front surface. It should be noted that the T tomogram of the cross section, Fig. 13, is much better than the BP tomogram and gives the actual contrast and size of the defect, as seen from comparing Figs. 13(b) and 11(b). It can be argued that the surface integral term in Eq. (7) is much less important in transmission,[25] since the reflected and heavily dumped thermal waves will have to cover twice the distance, $2l$, in order to contribute to the thermal-wave field at the back surface. Therefore the omission of the surface integral in Eq. (7) may be said to be *a posteriori* justified, with the volume integral representing the pseudopropagating field satisfactorily. A review of the tomograms in Figs. 12 and 13 leads to the conclusion that in thin samples for which inequality (31) does not hold rigorously, reconstructions of deep defects from T data are superior to those from BP data. The object function of the same thickness aluminum strip including a shallow defect is shown in Fig. 14. In this situation the reconstruction results exhibit opposite trends to those shown in Figs. 12 and 13: The BP tomogram, Fig. 15, is of very good quality and contrast, as expected from this tomographic mode's ability to reproduce accurate shallow defects (see also Fig. 3). On the other hand, the T reconstruction, Fig. 16, is only of fair quality, with adequate contrast, but with distorted (broadened) dimensions. The degree of distortion is

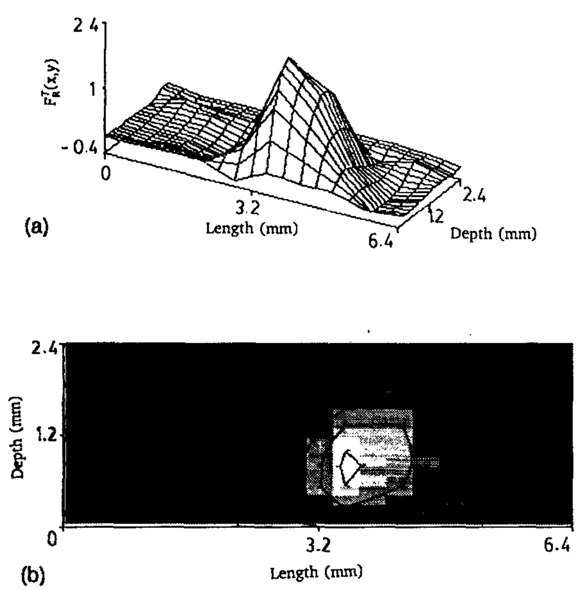

FIG. 16. (a) TSDT transmission reconstruction of the object function $F(x,y)$ of Fig. 14. Parameters similar to Fig. 15. (b) Top-down view showing isometric contours. Regularization parameter $\sigma=10^{-9}$.

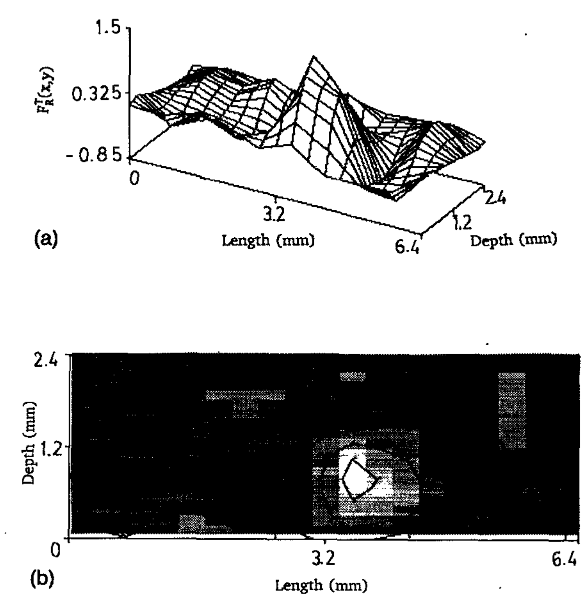

FIG. 18. Similar to Fig. 16 with beam intensity modulation frequency equal to 80 Hz. Regularization parameter $\sigma=10^{-7}$.

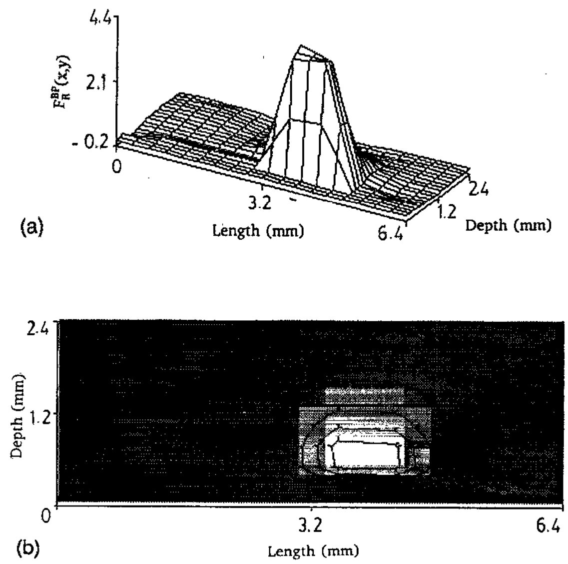

FIG. 19. Similar to Fig. 17 with beam intensity modulation frequency equal to 10 Hz. Regularization parameter $\sigma = 10^{-9}$.

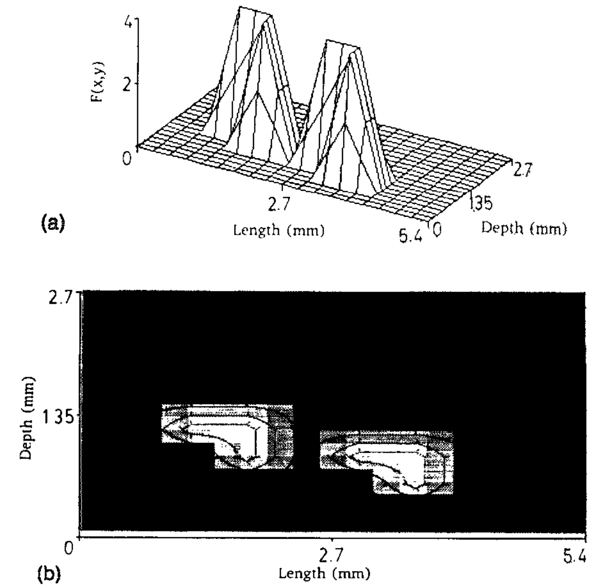

FIG. 21. (a) Three-dimensional relief of a simulated cross section of an aluminum strip of thickness 2.7 mm and width 5.4 mm, with two ellipsoidal airgap holes centered at $(x_c^1, y_c^1) = (3.6$ mm, 0.9 mm) and $(x_c^2, y_c^2) = (1.8$ mm, 1.2 mm). Dimensions of both holes: $(a,b) = (0.6$ mm, 0.3 mm). (b) Top-down view of the cross section, showing isometric contours.

lower than that observed with a thick sample [compare Figs. 16(b) and 4(b)], and the cause of it must be sought in the large distance between the location of the defect and the back surface of the sample.

In another simulation set we investigated the effect of the laser-beam modulation frequency variation on the tomographic reconstruction. Figure 17 is the BP reconstruction of Fig. 14 when the frequency is raised to 80 Hz. Only slight changes can be discerned in the higher frequency image. The degree of quality, contrast, and size reproduction is essentially the same, with a noticeable noise increase, as seen from comparing Figs. 15(a) and 17(a). The quality of the T reconstruction, Fig. 18, however, has undergone dramatic deterioration in all aspects of reconstruction, as seen from comparing Figs. 18 and 16. Therefore, shallow defects appear to require low frequencies to yield improved tomograms, in effect relaxing the thermally thick condition of inequality (31). When the frequency was decreased to 10 Hz, Fig. 19, an improvement in the BP reconstruction was observed, especially the background noise suppression. On the other hand, the T reconstruction, Fig. 20, has broadened considerably with comparison to the 30 Hz reconstruction, Fig. 16, with an overall degradation in image quality. It is clear that the defect can be delineated better under T reconstruction with the use of high enough

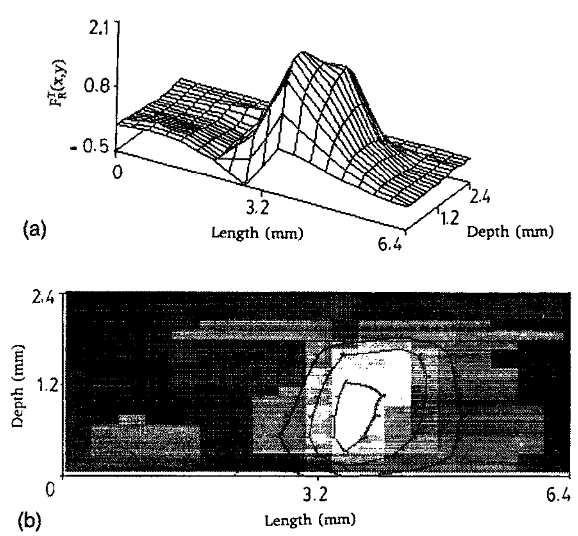

FIG. 20. Similar to Fig. 18 with beam intensity modulation frequency equal to 10 Hz. Regularization parameter $\sigma = 10^{-9}$.

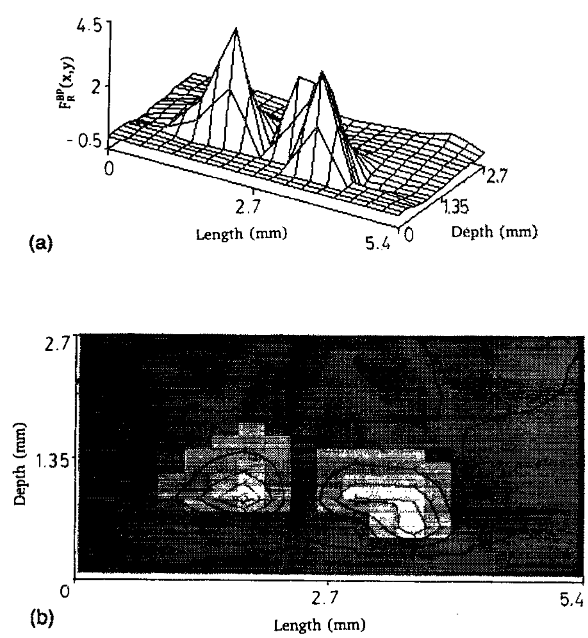

FIG. 22. (a) TSDT backpropagation reconstruction of the object function $F(x,y)$ of Fig. 21. Laser-beam position at $x_f = 2.4$ mm (point source). Beam intensity modulation frequency: 20 Hz. Trapezoidal rule of integration using the Born approximation. (b) Top-down view showing isometric contours. Regularization parameter $\sigma = 0$.

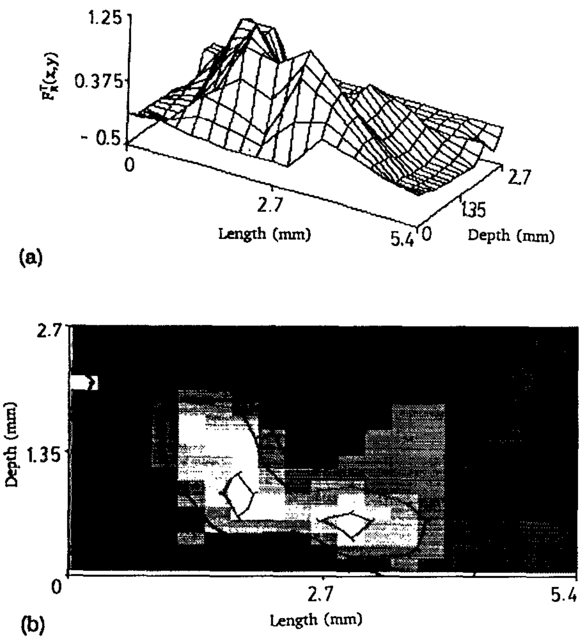

FIG. 23. (a) TSDT transmission reconstruction of the object function $F(x,y)$ of Fig. 21. Parameters similar to Fig. 22. (b) Top-down view showing isometric contours. Regularization parameter $\sigma=0$.

frequency to contain thermal-wave diffraction effects.[9,25] This frequency must be at the same time low enough to overcome degraded signal-to-noise ratios, Figs. 16, 18 and 20.

We further explored the ability of computational TSDT to reconstruct multiple defect structures within the thermal wavelength $\lambda_t(\omega)$. This amounts to defect interactions and the conditions of resolving neighboring defect

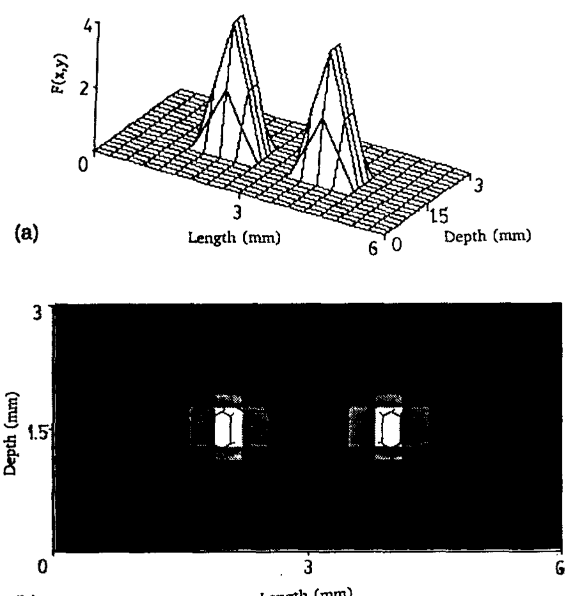

FIG. 24. (a) Three-dimensional relief of a simulated cross section of an aluminum strip of thickness 3 mm and width 6 mm, with two ellipsoidal airgap holes centered at $(x_c^1,y_c^1)=(4\text{ mm}, 1.4\text{ mm})$ and $(x_c^2,y_c^2)=(2\text{ mm}, 1.6\text{ mm})$. Dimensions of both holes: $(a,b)=(0.5\text{ mm}, 0.3\text{ mm})$. (b) Top-down view of the cross section, showing isometric contours.

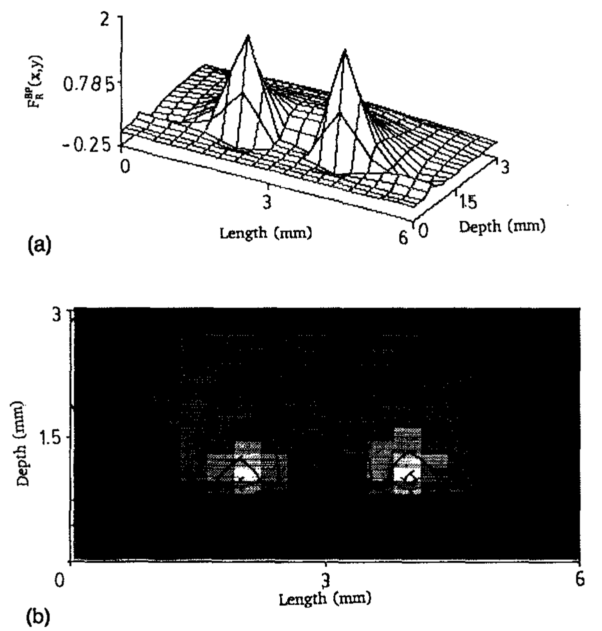

FIG. 25. (a) TSDT back-propagation reconstruction of the object function $F(x,y)$ of Fig. 24. Laser-beam position at $x_f=2.4$ mm (point source). Beam intensity modulation frequency: 2 Hz. Trapezoidal rule of integration using the Born approximation. (b) Top-down view showing isometric contours. Regularization parameter $\sigma=0$.

geometries. Figure 21 shows the input object function: an aluminum sample of thickness 2.7 mm with two ellipsoidal defects in close proximity to each other. BP reconstruction under an $f=20$ Hz laser thermal-wave excitation is shown in Fig. 22. No nonzero regularization parameter was used for this reconstruction, which resolves the two defects fairly well, even though only a single source position was used. All three: magnitude (contrast), size, and depth are

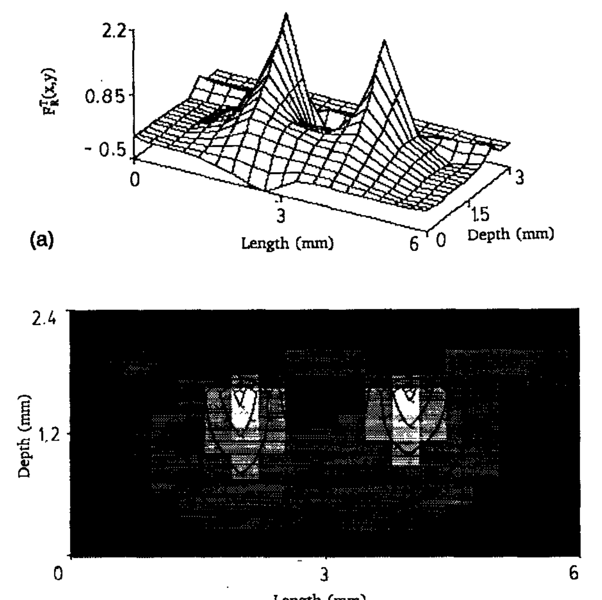

FIG. 26. (a) TSDT transmission reconstruction of the object function $F(x,y)$ of Fig. 24. Parameters similar to Fig. 25. (b) Top-down view showing isometric contours. Regularization parameter $\sigma=10^{-13}$.

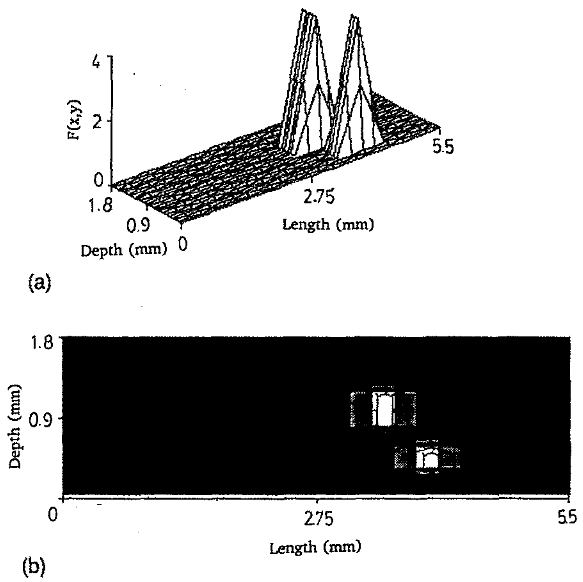

FIG. 27. (a) Three-dimensional relief of a simulated cross section of an aluminum strip of thickness 1.8 mm and width 5.5 mm with two ellipsoidal airgap holes centered at $(x_c^1, y_c^1) = (4\text{ mm}, 0.4\text{ mm})$ and $(x_c^2, y_c^2) = (3.5\text{ mm}, 1\text{ mm})$. Dimensions of both holes: $(a,b) = (0.5\text{ mm}, 0.2\text{ mm})$. (b) Top-down view of the cross section, showing isometric contours.

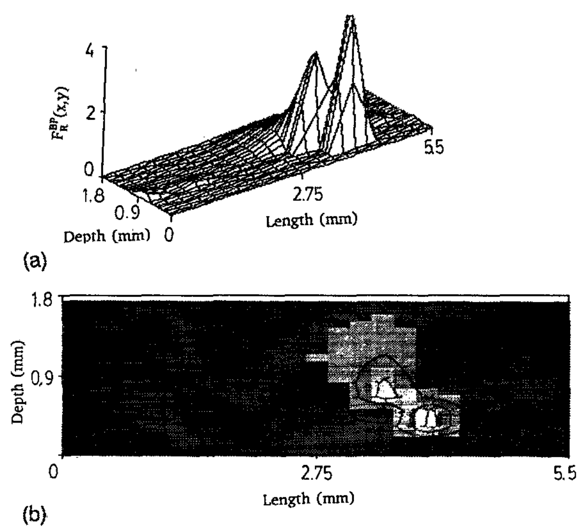

FIG. 28. (a) TSDT backpropagation reconstruction of the object function $F(x,y)$ of Fig. 27. Laser-beam position at $x_f = 2.4$ mm (point source). Beam intensity modulation frequency: 2 Hz. Trapezoidal rule of integration using the Born approximation. (b) Top-down view showing isometric contours. Regularization parameter $\sigma = 0$.

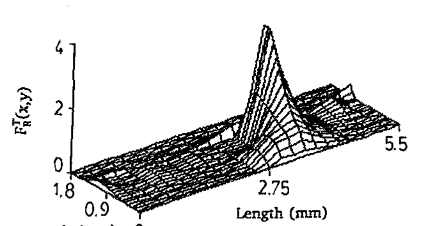

FIG. 29. TSDT transmission reconstruction of the object function $F(x,y)$ of Fig. 27. Parameters similar to Fig. 28. Regularization parameter $\sigma = 0$.

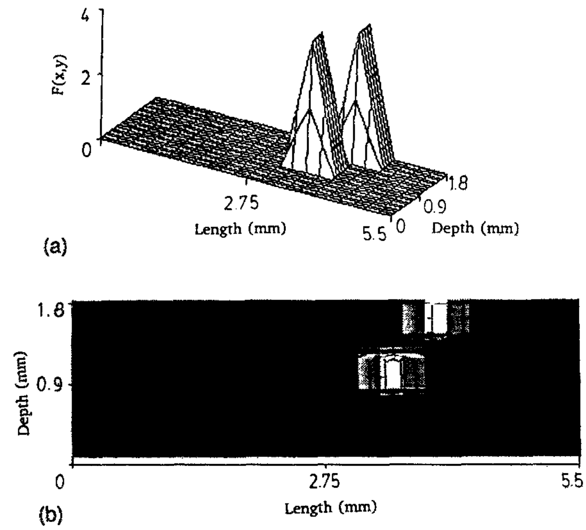

FIG. 30. (a) Three-dimensional relief of a simulated cross section of an aluminum strip of thickness 1.8 mm and width 5.5 mm, with two ellipsoidal airgap holes centered at $(x_c^1, y_c^1) = (3.5\text{ mm}, 1\text{ mm})$ and $(x_c^2, y_c^2) = (4\text{ mm}, 1.6\text{ mm})$. Dimensions of both holes: $(a,b) = (0.5\text{ mm}, 0.2\text{ mm})$. (b) Top-down view of the cross section, showing isometric contours.

reconstructed with high fidelity, owing to the shallowness of the defects. In contrast to the good quality of the BP reconstruction, the T reconstruction, Fig. 23, is very unsatisfactory, with severe distortions, including defect merging and obliteration of the interdefect boundary.

It is interesting to note that when the defect pair moves deeper into the bulk of the sample and their relative distance increases, as shown in Fig. 24, then both BP and T reconstructions yield sufficiently good images, Figs. 25 and 26, respectively. In this set of reconstructions the frequency f was lowered to 2 Hz to allow for thermal thinness of the imaged subsurface slice.[24,25] As a result the resolution of both BP and T tomograms is adequate, with the latter exhibiting more background noise, as well as some depth distortions of the defects, Fig. 26(b). The BP image, however, is depth-distortion-free, Fig. 25(b). *In summary, Figs. 21–26 indicate that in both cases of shallow and deep defect pairs, which are otherwise at approximately the same depth, BP tomography yields superior reconstructions.*

The final set of tomograms that we studied in this work is related to subsurface defect pairs at different depths,

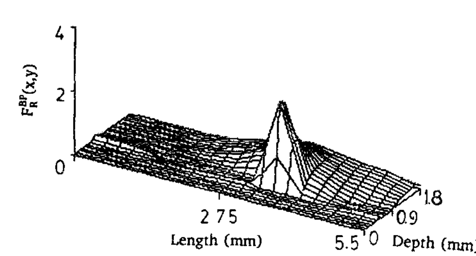

FIG. 31. TSDT backpropagation reconstruction of the object function $F(x,y)$ of Fig. 30. Laser-beam position at $x_f = 2.4$ mm (point source). Beam intensity modulation frequency: 2 Hz. Trapezoidal rule of integration using the Born approximation. Regularization parameter $\sigma = 0$.

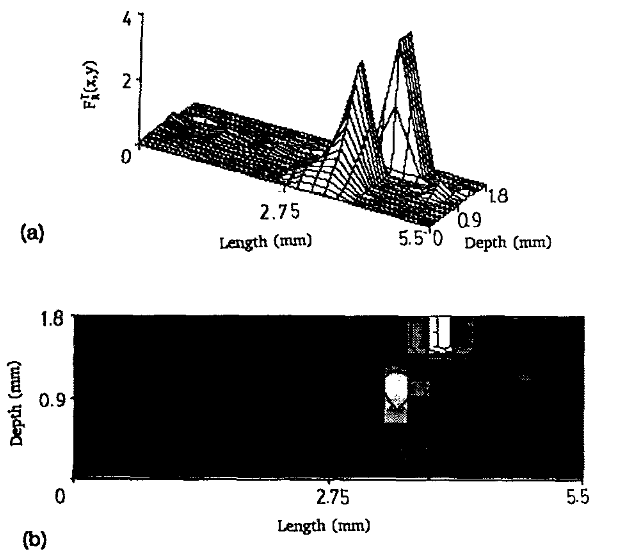

FIG. 32. (a) TSDT transmission reconstruction of the object function $F(x,y)$ of Fig. 30. Parameters similar to Fig. 31. (b) Top-down view showing isometric contours. Regularization parameter $\sigma=0$.

with partial spatial overlap along the "line of sight" between a single laser source position and some position of the detector coordinate, x_l. One such input object function $F(x,y)$ is shown in Fig. 27. In Fig. 28 we show the BP reconstruction from a laser source position to the left of both defects (note the relief-plot rotation in this case, compared to earlier figures, to show the interdefect "valley"). It is seen that the depth, sizes, and magnitudes of the defects are reproduced satisfactorily, with the magnitude (contrast) of the deeper defect being marginally degraded compared to that of the shallower defect, as expected. It is further interesting to note that the low frequency used (2 Hz) does not severely limit spatial resolution of the defects, which might be expected due to the considerable thermal-wave diffraction present at low f. Contrary to the BP reconstruction, the T reconstruction exhibits severe loss of resolution, defect merging, and almost complete screening of the shallow (upper) defect by the dominant deep (lower) defect, Fig. 29. The size, position, and magnitude of the lower defect, however, are well reconstructed. It is clear that transmission tomography yields a weighted defect image with the dominant defects being those close to the back surface. If the pair of defects is located very close to the back surface, Fig. 30, then the opposite situation arises. The BP reconstruction is almost entirely dominated by the shallow defect, whereas defect merging and screening of the deeper defect is observed, Fig. 31. On the other hand, the T reconstruction, Fig. 32, is quite good and accurately reproduce the depth, size, and contrast of the two defects, with some distortion in the back shadow of the upper defect. Clearly, this tomographic mode should be used with samples involving deep defects in close proximity.

V. INHERENT FEATURES OF COMPUTATIONAL TSDT

The extensive simulations and tomographic reconstructions presented above lead to the following set of empirical "rules" governing thermal-wave slice diffraction tomography:

(1) The Born approximation seems to yield a large number of satisfactory results, even for defects with thermal diffusivities very different from that of the background solid material.

(2) Shallow defects in thermally thick samples are imaged better with BP reconstruction. Deep defect BP reconstruction is also of higher fidelity than T reconstruction, albeit in the presence of considerable background noise.

(3) In thermally intermediate samples, deep defects appear distorted under both reconstruction modes, however, T reconstruction produces higher contrast.

(4) In thinner samples than those of case (3) above, deep defects close to the back surface are imaged better with T reconstruction. Shallow defects are imaged much better with BP reconstruction.

(5) Increasing the laser-beam source modulation frequency causes small changes in the BP reconstruction, while it leads to marked deterioration of the T reconstruction of shallow defects.

(6) Pairs of defects in close proximity and at the same (approximate) depth in a thin sample are only imaged with satisfactory spatial resolution using BP reconstruction, when they are shallow. There is a trade-off between increased interdefect distance and increased depth in preserving spatial BP tomogram resolution; BP tomogram reconstructions gradually degrade, whereas T reconstructions improve with increased depth.

(7) Shallow defect pairs at different depths reconstruct only with BP tomography. Deep defect pairs at different depths reconstruct only with T tomography.

ACKNOWLEDGMENT

The authors wish to acknowledge the partial support of the Natural Sciences and Engineering Research Council of Canada (NSERC), which made this work possible.

[1] A. Mandelis and M. Mieszkowski, U.S. Patent No. 4,950,897, August 1990.
[2] M. Munidasa and A. Mandelis, J. Opt. Soc. Am. A **8**, 1851 (1991).
[3] M. Munidasa, A. Mandelis, and C. Ferguson, Appl. Phys. A **54**, 244 (1992).
[4] A. Mandelis, J. Phys. A **24**, 2485 (1991).
[5] A. C. Kak and M. Slaney, *Principles of Computerized Tomographic Imaging* (IEEE Press, New York, 1988).
[6] O. Padé and A. Mandelis, Inverse Problems (in press).
[7] M. Mieszkowski, K. F. Leung, and A. Mandelis, Rev. Sci. Instrum. **60**, 306 (1989).
[8] G. T. Herman, A. Lent, and S. W. Rowland, J. Theor. Biol. **42**, 1 (1973).
[9] A. Mandelis, J. Opt. Soc. Am. A **6**, 298 (1989).
[10] P. M. Morse and H. Feshbach, *Methods of Theoretical Physics* (McGraw-Hill, New York, 1953), Chap. 7.
[11] K. J. Langenberg, *Applied Inverse Problems*, Notes on Summer School on Applied Inverse Problems (Fachgebiet Theoretische Elektrotechnik der Gesamthochschule, Kassel, GhK-TET, Kassel, 1986) Chap. 3.
[12] L. D. Favro, P. K. Kuo, and R. L. Thomas, in *Photoacoustic and Thermal Wave Phenomena in Semiconductors*, edited by A. Mandelis (North-Holland, New York, 1987), Chap. 4, p. 75.
[13] D. Nahamoo, S. X. Pan, and A. C. Kak, IEEE Trans. Sonics Ultrason. **SU-31**, 218 (1984).
[14] E. Kreyszig, *Advanced Engineering Mathematics*, 7th ed. (Wiley, New York, 1993), Chap. 18.
[15] M. Abramowitz and I. Stegun, *Handbook of Mathematical Functions*, 9th ed. (National Bureau of Standards, Washington D.C., 1970).

[16] R. K. Mueller, M. Kaveh, and G. Wade, Proc. IEEE **67**, 567 (1979).
[17] Y. S. Touloukian, R. W. Powell, C. Y. Ho, and M. C. Nicolaou, *Thermal Diffusivity* (IFI/Plenum, New York, 1973).
[18] M. Kaveh, M. Soumekh, and R. K. Mueller, in *Acoustical Imaging*, edited by J. Powers (Plenum, New York, 1981), Vol. 10.
[19] M. Kaveh, M. Soumekh, Z. Q. Lu, R. K. Mueller, and J. F. Greenleaf, in *Acoustical Imaging*, edited by E. A. Ash and C. R. Hill (Plenum, New York, 1983), Vol. 12, p. 599.
[20] G. Hämmerlin and K. H. Hoffman, *Numerical Mathematics* (Springer, New York, 1991).
[21] R. Kress, *Linear Integral Equations* (Springer, New York, 1989).
[22] B. Hofmann, *Regularization for Applied Inverse and Ill-Posed Problems* (Teubner, Leipzig, 1986).
[23] B. T. Smith, J. M. Boyle, J. J. Dongara, B. S. Garbow, Y. Ikebe, V. C. Klema, and C. B. Moler, *Matrix Eigensystem Routines—EISPACK Guide*, 2nd ed., Lecture Notes in Computer Science Vol. 6 (Springer, New York, 1976).
[24] A. Rosencwaig and A. Gersho, J. Appl. Phys. **47**, 64 (1976).
[25] A. Mandelis and K. F. Leung, J. Opt. Soc. Am. A **8**, 186 (1991).